Saudi Journal of Biological Sciences 29 (2022) 2447–2454

Contents lists available at ScienceDirect

Saudi Journal of Biological Sciences

journal homepage: www.sciencedirect.com

Original article

Sensing mammographic density using single-sided portable Nuclear Magnetic Resonance

Maher Alqurashi [a], Konstantin I. Momot [b,c], Ali Aamry [d], H.I. Almohammed [e], Hussin Aamri [f], Yehia H. Johary [g], Fouad A. Abolaban [h], Abdelmoneim Sulieman [i,*]

[a] Radiology Department, Ministry of Health, Riyadh, Saudi Arabia
[b] School of Chemistry, Physics and Mechanical Engineering, Queensland University of Technology (QUT), Brisbane, Australia
[c] Institute of Health and Biomedical Innovation, Queensland University of Technology (QUT), Brisbane, Australia
[d] Nuclear Medicine Department, King Saud Medical City, Riyadh, Saudi Arabia
[e] Department of Radiological Sciences, College of Health and Rehabilitation Sciences, Princess Nourah Bint Abdulrahman University, P.O Box 84428, Riyadh 11671, Saudi Arabia
[f] Medical Physics Department, King Saud University Medical City (KSUMC), Riyadh, Saudi Arabia
[g] Medical Physics Department, General Directorate of Health Affairs in Aseer Region, Abha, Saudi Arabia
[h] Nuclear Engineering Department, Faculty of Engineering, King Abdulaziz University, P. O. Box 80221, Jeddah 21589, Saudi Arabia
[i] Radiology and Medical Imaging Department, College of Applied Medical Sciences, Prince Sattam Bin Abdulaziz University, P.O. Box 422, Alkharj 11942, Saudi Arabia

ARTICLE INFO

Article history:
Received 17 August 2021
Revised 5 December 2021
Accepted 9 December 2021
Available online 16 December 2021

Keywords:
NMR
MRI
Relaxation time
Breast cancer
Mammographic density

ABSTRACT

This research paper presents a quantitative approach to sensing mammographic density (MD) using single-sided portable Nuclear Magnetic Resonance (NMR). It focuses on three main techniques: spin–lattice relaxation (recovery) time (T_1), spin–spin relaxation (decay) time (T_2), and Diffusion (D) techniques by testing whether or not the aforementioned techniques are in agreement with the gold standard and with each other when used for scanning breast tissue specimens with a variety of mammographic densities (MDs). The high mammographic density (HMD), intermediate MD, and low mammographic density (LMD) regions of each slice were identified according to the mammogram images. Subsequently, the grayscale values for these regions were quantified. One region was measured from the first sample while the remaining ones were measured from the second sample. The same areas were then exposed to portable NMR, and the sequences used as following: the stimulated echo sequence for diffusion (D), the Carr-Purcell-Meiboom-Gill (CPMG) sequence for T_2, and saturation recovery sequence for T_1. The correlations between the grayscale values and NMR techniques were strongly correlated. The Pearson correlation coefficient, R, of T_1 (%) versus grayscale value, D (%) versus grayscale value, and T_2 (%) versus grayscale value, was 0.91, 0.91, and 0.93, respectively. Furthermore, the relative water content of the breast slices based on T_1, T_2, and diffusion (D) measurements were strongly in agreement with each other. The Pearson correlation coefficient, R, of D (%) versus T_1 (%), D (%) versus T_2 (%), and T_1 (%) versus T_2 (%), was 0.984, 0.966, and 0.9868, respectively. The three pulse sequences can be employed in a portable NMR device to deliver continuous quantitative measurements of MD in breast tissue samples. As a result, the method demonstrated to be acceptable for determining the distribution of MDs among breast tissue samples without the need for additional qualitative analysis.

1. Introduction

Breast cancer (BC) is caused by numerous risk factors that occur in isolation (Britt et al., 2020; Tourell et al., 2018). The most popular ones include, high post-menopausal body mass index (BMI), ageing (Tyrer et al., 2004), oral contraceptives, less breast feeding, congenital factors (family history of the disease), high mammographic density (MD), exposure to ionizing radiation, and early menstrual occurrences (early menarche) at the age of 11 years and below (Tamam et al., 2021; Bell, 2020; National Health and

* Corresponding author.
E-mail address: a.sulieman@psau.edu.sa (A. Sulieman).
Peer review under responsibility of King Saud University.

Production and hosting by Elsevier

https://doi.org/10.1016/j.sjbs.2021.12.022
1319-562X/

Medical Research Council, 2018, Brinton et al., 2018; Sulieman et al., 2019). Sung et al estimated that the incidence of breast cancer is 2.3 million new cancer cases representing 11.7% of all cancer incidence worldwide (Sung et al., 2021). For women aged 50–69, BC screening is suggested every one to two years. For high-risk females, an MRI of the breast is also indicated (Niell et al., 2017). Regardless of ethnicity, it was revealed that roughly 30% of patients under the age of 30 have fatty breasts, and around 25% of patients over 70 have DB. Breast density was higher in groups younger than 50 years old, while older ladies had a tendency to have reduced breast density (Salem et al., 2017; Liu et al., 2014). However, elimination of breast cancer risk is possible through awareness improvement, effective health services and reduction of the stress (Karim et al., 2019). MD is considered as the strongest indicator of BC risk (Cil et al., 2010). It is defined as the level of radiodense fibroglandular deposits in breast tissues (Shang et al., 2021; Kopans, 2009). The hyper- intense region on a mammographic image is indicative of high MD, with high levels of fibroglandular tissue (FGT) (Tourell, et al., 2018; Bell, 2020). Most of the women within the age bracket of 40–75 years exhibit high levels of MD. This means that they are more likely to be at risk of breast cancer than women in other age groups (Huang, 2018). It is important to accurately estimate an individual's MD at the early stages of manifestation to facilitate risk evaluation and prognosis of BC (Collaborative Group on Hormonal Factors in Breast Cancer, 2012). Research reveals that the risk exposure of an Australian woman to BC over their entire lifetime is in every 8 or about 12.5% (AIHW, 2017). This figure is comparable to that of the United Kingdom (12.5%) and that of the United States of America (12%). On average, approximately 500,000 deaths arising from BC complications have been reported recently from the 14 million detected cases of BC; an indication of the severity of the global BC contraction (Ghosh et al., 2011; National Cancer Institute, 2017). Studies conducted in the recent past have shown that MD has a direct impact on the progression and spread of BC cells (Aiello et al., 2005; Eriksson et al., 2013a). The radio-dense regions on a mammogram (high MD regions) correlate to FGT (collagen stroma) zones and display a white appearance. On the contrary, radiolucent zones (low MD regions) are rich in adipose tissues and are dark in appearance (Ghosh et al., 2011). Research suggests that collagens and proteoglycans are key determinants of MD (Ghosh et al., 2011; Huo et al., 2015). Breast density has a significant impact on the sensitivity of mammograms for the identification of BC. Mammogram sensitivity ranges from 80 to 98 percent for women with fatty breasts while the sensitivity drops to 30–65 percent for women with thick breasts (Butler, 2015). Typically, the Breast Imaging Reporting and Data System (BI-RADS) is a viable tool for classifying MD in breast tissues. For example, dense tissues are represented as BIRADS > 75% (Sickles, 2013). In such cases, the utility of mammography diminishes as a breast cancer detection tool. Based on the BI-RADs scale, women in the upper MD quartile have about 5 times higher chances of exposure to BC compared to those in the lower quartile (McCormack & Silva, 2006). It has been suggested that dense tissue concentration in the breast is influenced by single nucleotide polymorphism, estrogen fluctuations stereotypical during the menstrual cycle, and onset of menopause (White et al., 1998; Stone et al., 2006). Other than physiological factors, lifestyle factors that affect MD include alcohol abuse (which increases MD), one's diet, engagement in physical activities (reduces MD), and lack of parity (increases MD). More so, the above indicators suggest that MD evolves overtime (Brentnall et al., 2015). As such, MD- related BC risk can be modified (Woolcott et al., 2012). This can be achieved by monitoring MD iteratively to reveal individual-specific risks to BC (Eriksson et al., 2013b).

Nuclear Magnetic Resonance (NMR) technique is based on the fact that in living tissues have plenty of protons mainly in water and fat molecules whose nuclei contain positively charged protons with a net spin and consequently, an intrinsic induced magnetic field around them. The MRI image contrast is determined by regions of low (hypointense – black) and high (hyper-intense/white) signal intensities (Dale et al., 2015). The shades of grey reflect regions of intermediate signal intensity. Image contrast is attributed to three primary mechanisms: the proton density (PD) of hydrogen within a tissue, T_2, and T_1. For example, in T_2-weighted image, tissues with considerable levels of the transverse coherent magnetization components tend to create hyper-intense regions on the image scan. In tandem, the NMR coil receives a high amplitude signal output. In contrast, tissues with low or no levels of coherent transverse magnetization at a time TE, tend to return a low amplitude signal. Diffusion (D), T_1 and T_2 parameters in the portable NMR can be used to improve the quantification of MD as a risk factor for breast cancer. The time constants, T_1 and T_2 are derived from the high and low MD domains (LMD and HMD) of digital slice mammography (Danieli & Blümich, 2013). T_2 measurements, unlike T_1, reveal the water-to-fat (w/f) ratio of a breast tissue (Ali et al., 2019), and the both techniques provide accurate discrimination between HMD and LMD regions in the breast tissue samples (Tourell et al., 2018). Indeed, Tourell et al. (2018) concluded that the difference between the HMD and LMD regions of both excised and full breast tissues was statistically significant, where $p < 0.001$. The samples were obtained from BC patients undergoing prophylactic mastectomy. In this study, the CPGM decay curves for T_2 were constructed using Inverse Laplace Transformation (ILTs). The T_2 spectra of both the LMD and HMD regions revealed two distinct water and fat peaks, which were further revealed statistically significant differences ($p < 0.005$) via t-paired tests (Tourell et al., 2018). Recently, Huang et al. (2018) measured samples of breast tissues with dissimilar MDs. The investigators extracted volumetric MD image for 10 samples of breast tissues through μCT. In this study, the saturation recovery sequence for T_1, CPMG sequence for T_2, and stimulated sequence for diffusion were applied on the samples with the aid of the portable PM25 model of the NMR. The continuous distribution of MDs scale for the excised samples ranged between zero and 100%. The "gold standard" for the experiment was the μCT. HMD% measured on the μCT scale showed impressive correlations with T_1 and diffusion data, where R was ~0.92 and 0.96 respectively. Furthermore, the linear correlation between NMR-assisted water diffusion and T_1 data was impressive; R was ~0.94 while the correlation between T_2 and diffusion data was modest due to an overlap of the water and fat peaks in the T_2 spectra. If TE is poorly selected, such that it becomes too short, then the fat and water peaks will overlap in the spectra of T_2 (Huang, 2018). However, by selecting moderately long TE, the NMR probe could provide reliable MD measurements. This study will investigate whether or not the three techniques T_1, T_2, and diffusion (D) are in agreement with each other as well as in agreement with the gold standard (Mammogram images) when used for scanning breast tissue samples with a range of mammographic densities (MDs). To establish the concurrence, the conclusion will be derived from six charts (T_1 (%) vs grayscale value), (D (%) vs grayscale value), (T_2 (%) vs grayscale value), (T_1 vs T_2), (T_1 vs D) and (T_2 vs D), which will show how well the accuracy reproducibility of three techniques compared to mammogram images (gold stander) of the two samples.

2. Material and methods

2.1. Slice mammogram measurements

In this study, 2 slices of breast tissues mammogram images were obtained from two different participants (women) undergo-

ing prophylactic mastectomy with the view of preventing breast cancer, or breast reduction surgery. The HMD, intermediate MD, and LMD regions for the two mammogram images were labelled by the radiologist at the Princess Alexandra Hospital. Subsequently, the grayscale values of the six regions in the two samples were obtained using MATLAP software. The experimental parameters for NMR probing are summarized in Table 1. The two slices were frozen at −80 °C at Translation Research Institution (TRI) before being transferred to portable NMR room. Subsequently, the samples were left one hour at room temperature (24 °C) in order to be deforested. The study has been approved by the Peter MacCallum Human Research Ethics Committee (#08/21), Metro South Hospital and Health Services, Queensland (HREC/16/QPAH/107) and Mater Research (RG-16–028-AM02, MR-2016–32), and administratively approved by QUT (#1600000261).

2.2. Single-sided NMR-mouse setup

The NMR measurements were performed using the single-sided NMR (PM 25 - Magritek, Wellington, New Zealand). The setup shown in Fig. 1 has a RF surface coil that stimulates and detects the NMR signal. The magnetic field gradient (g) is permanently installed in the orthogonal direction of the permanent horizontal magnetic field (B_o). The magnetic field gradient is equivalent to 7.5 $T.m^{-1}$ while Bo is 0.31 T. The portable single-sided NMR instrument has a translation stage that calibrates the sensor to the desired sensing depth. The effective depth of penetration of the PM25 probe is 25 mm. The size of the horizontal sensing slice is dependent on the coil's dimensions; the thickness of the slice varies depending on the amplitude of the applied magnetic field gradient and the strength of the RF magnetic field (Ali, 2018). In this setup (Fig. 1), the excitation frequency (RF) can be scaled to achieve spatial localization of the samples.

2.3. Quantifying mammographic density (MD)

The stimulated echo sequence for diffusion (D), the Carr-Purcell-Meiboom-Gill (CPMG) sequence for T_2, and saturation recovery sequence for T_1 were applied sequentially for the same six regions.

2.3.1. T_1 Measurements

A saturation recovery sequence was applied to generate the full T_1 recovery curve for each region. This sequence provided a train of 90° RF pulses to counteract the strong inhomogeneity of the magnetic field and to zero the longitudinal magnetization components (Catherine and John, 2019). Each T_1 curve was sampled at 30 values of the saturation recovery times TSR. Then, the Carr- Purcell-Meiboom-Gill sequence was used to sense signals (Bluemich and Perlo, 2008). The relative amount of water and fat signals for each region were measured using a 2-parameter non-linear biexponential least-squares fit (LSF) of equation (2) below:

$$(t) = K + S_0 e^{-t/T_1} a + S_1 e^{t/T1} b \quad (1)$$

where S_0 is the relative amount of water; T_1 a is the recovery time of water molecules;

Table 1
Experimental parameters.

Maximum depth of penetration	25 mm (NMR-Mouse PM25)
Gold standard	Mammogram
Number of scanned regions	1 region at 5.9 mm depth from the first sample, 5 regions at 4.5 mm depth from the second sample
Output	Distribution of MDs

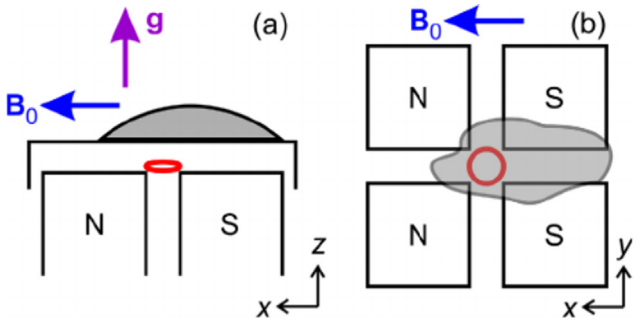

Fig. 1. Portable NMR Mouse (Tourell, et al., 2018). (a) The side view demonstrates the permanent magnets N & S, direction of static magnetic field as well as the direction of static gradient. The red circle represents the sensing region, while the gray slice denotes the sample's position; (b) is the top view of the instrument.

S_1 is the amplitude of fat content, and T_1 b is the recovery time of fat molecules.

The data analysis was performed using *Wolfram Mathematica* program, and the code was written by Momot (2019).

For each region, the following parameters were set for T_1 sequence (Table 2).

2.3.2. T_2 Measurements

2.3.2.1. Analytical framework. The *Carr-Purcell-Meiboom-Gill* (CPMG) was used to obtain the CPMG decay for the six regions along the two samples. However, the first and second scans failed to resolve between water and fat peaks because the echo times (TEs) were short, TE = 150 μs and 300 μs respectively. Then, the same region was scanned again with TE = 700 μs which succeeds to resolve the two peaks. This TE value was adopted for scanning the remaining regions. The curves are shown in the results section. For each region, the following parameters were set for T_2 (Table 2):

Worth noting, The Inverse Laplace Transformation (ILT) was used to reconstruct the T_2 spectra which displayed the amplitudes or peaks of fat and water. Equation (2) below shows T_2 multicomponent decay (Ali et al., 2019):

$$S(t_j) = g_j \sum_{i=1}^{m} A(T_i)\exp\left(-\frac{t_j}{T_j}\right) + \in_j \quad (2)$$

where $\in_j$ represents the noise; the amplitudes of relaxation peak are represented by positive values of $A(T_i)$, $i = 1...m$ represents the # of relaxation-time items in the time T_i, which is a time constant for relaxation. $A(T_i)$ was obtained by inverting the T_2 curve. This was achieved by employing the least-square algorithm to minimize x^2 as shown below in equation (3) (Ali et al.,2019).

$$\min\{x^2\} = \sum_{i=1}^{n} g_j - \sum_{i=1}^{m} A(T_i)\exp\left(-\frac{t_j}{T_i}\right)^2 \quad (3)$$

Given that noise is an inherent property of the NMR signal, the smoothing parameter α was normalized as shown in equation (4) (Ali et al., 2019):

$$\min\{x^2\} = \sum_{i=1}^{n} g_j - \sum_{i=1}^{m} A(T_i)\exp\left(-\frac{t_j}{T_i}\right)^2 + \frac{1}{\sigma}\sum_{i=1}^{m}(2A(T_i) - A(T_{i=1}) - A(T_{i+1})^2 \quad (4)$$

The code that was initially written by Venkataramanan et al. (2002) was used to solve equation (3) in MATLAB program. The procedure above was repeated for all the T_2 distributions for each region in the two samples to minimize their sensitivity to noise.

Table 2
Parameter settings for the T_1 technique.

Saturation recovery sequence				CPMG block		
Eacho time (TE) (μs)	Repetition time (ms)	Max recovery time (ms)	Number of echos	Number of complex points	Number of scan	Dwell time (μs)
60	2000	3000	64	16	4	0.5

The corresponding area fractions of the two peaks (fat and water) in each of the T_2 distributions were analyzed as shown in equation (6) (Ali et al., 2019):

$$AF_W = \frac{A_W}{A_W + A_W} \tag{5}$$

where AF_W is area fraction for water; A_W is the amplitude of the water (first peak), and A_W is the amplitude of the fat (second peak)

Similarly,

$$AF_F = \frac{A_F}{A_F + A_F} = 1 - AF_W \tag{6}$$

where AF_F is area fraction for fat; A_F is the amplitude of the fat (second peak), and A_W is the amplitude of the water (first peak).

2.3.2.2. Diffusion measurements. A stimulated echo sequence was applied, while the CPMG block was coupled for detection. The diffusion interval Δ was set at 10 ms, while δ was varied from 0.05 ms to 1 ms with 32 step points. Subsequently, the diffusion curve (signal versus δ) was plotted for each region. The relative apparent amounts of fat and water were quantified via a two-parameter biexponential least-squares fit of the following equation:

$$S = S_0 \cdot e^{-y^2 g^2 \delta^2 (\Delta - \delta/3) \times D} + S_1 \cdot e^{-y^2 g^2 \delta^2 (\Delta - \delta/3) \times D} \tag{7}$$

where S_0 and S_1 represent the amplitudes of water and fat, respectively, Δ is the diffusion interval, while δ denotes the path for longitudinal magnetization. Signals corresponding to fast and slow molecular diffusion are linked to water and fat components, in their respective order.

The data analysis was performed using *Wolfram Mathematica* program, and the code was written by Momot (Momot, 2019).

For each region, the following parameters were set (Table 4).

2.4. Statistics

For each graph, the Pearson correlation coefficient was calculated, and their P values were obtained as well.

3. Results

After setting the various parameters shown in Table 1 through Table 3 for the specified techniques, the relative amounts of water based on three techniques as well as the grayscale values were obtained for the 6 regions (Table 5). Figs. 2–7, show plots of T_1 data versus grayscale values, Diffusion results versus grayscale values, T_2 versus grayscale values, Diffusion versus T_1, and Diffusion versus T_2, and T_1 versus T_2, respectively, alongside their Pearson correlation coefficients. The regions of interest for the above images were highlighted as shown in Fig. 10 A and B. The graphical representative measurements are shown Fig. 11 for T_1 and the Diffusion (D) techniques, respectively. From Table 5, the results of region 6 refer to the first sample while the other regions data have been obtained from the second sample. In Fig. 11, the amplitude of the first four points represent the amount of water (fast diffusion). In contrast, the other points represent the amplitude of fat (slow diffusion). Fig. 2 shows a graphical plot of T_1 data (%) versus grayscale value. The Pearson Correlation Coefficient, R is 0.91 at 95% confidence interval, and p value = 0.0097 which is <0.05; therefore, the correlation is statistically significant. Fig. 3 shows a graphical linear plot of Diffusion (%) versus grayscale value. The Pearson Correlation Coefficient, R is 0.91 at 95% confidence interval, and the p value is 0.004 which is <0.05; therefore, the correlation is statistically significant. Fig. 4 shows a graphical linear plot of T_2 (%) versus grayscale data. The Pearson Correlation Coefficient, R ≈ 0.93 at 95% confidence interval, and the p value is 0.009 which is < 0.05; therefore, the correlation is statistically significant. Fig. 5 illustrates a graphical linear plot of Diffusion (%) versus T_1 (%). The Pearson Correlation Coefficient, R ≈ 0.97 at 95% confidence interval, and the p value is 0.004 which is <0.05; therefore, the correlation is statistically significant. Fig. 6 illustrates a graphical linear plot of T_2 (%) versus Diffusion (%). The Pearson Correlation Coefficient, R ≈ 0.95 at 95% confidence interval, and the p value is 0.004 which is <0.05; therefore, the correlation is statistically significant. Fig. 7 above illustrates a graphical linear plot of T_2 (%) versus T_1 (%). The Pearson Correlation Coefficient, R ≈ 0.99 at 95% confidence interval, and the p value is 0.0001 which is <0.05; therefore, the correlation is statistically significant (see Figs. 8 and 9).

4. Discussion

Breast MRI is used for early BC detection and patients with high BC risk. It has a higher temporal and spatial resolution and a better signal-to-noise ratio (NSR) than other imaging modalities such as mammography, positron emission tomography (PET), and ultrasonography. In addition, breast MRI has no risk of ionizing radiation exposure and enables simultaneous assessment of both breasts (Iranmakani, et al., 2020).

From the experimental results, it can be observed that the Pearson Correlation coefficients, R, of T_1 (%) versus Grayscale value, diffusion (%) versus Grayscale value, T_2 (%) versus Grayscale value, T_1 (%) versus diffusion (%), T_2 (%) versus diffusion (%), and T_2 (%) versus T_1 (%), was 0.91, 0.91, 0.93, 0.97, 0.95, 0.99 respectively at 95% confidence interval. In all cases, R > 90% and $p < \alpha$, implying that the correlations are statistically significant. This means the water content based on spin–lattice relaxation time T_1, spin–spin relaxation time T_2 and diffusion are in agreement with each other as well as in agreement with the gold standard. The amount of water based on diffusion increases proportionately with an increase in the water content based on T_1 and T_2 techniques. Clearly, the water content displayed an excellent quantitative correlation with the tissue content over the range of MDs investigated where higher MD in the mammogram images corresponds to higher water con-

Table 3
Parameter settings for the T_2 measurements.

Eacho time (TE) (μs)	Repetition time (ms)	Number of eachos	Number of complex points	Number of scan	Dwell time (μs)
700	7000	1500	32	8	0.5

Table 4
Parameter settings for Diffusion (D) measurement.

Stimulated sequence			CPMG block		
Eacho time (TE) (μs)	Repetition time (ms)	Number of eachos	Number of complex points	Number of scan	Dwell time (μs)
60	2000	64	32	8	0.5

Table 5
Summary of the results obtained from the six regions.

Region number	T_2 data (%)	Diffusion data (%)	T_1 data (%)	Grayscale Values
1	8.74	13.88	27.37	91.16
2	17.74	23.92	36.31	104.04
3	26.17	23.95	40.3	116.577
4	11.67	16.3	31.2	86.8
5	30.72	32.787	44.46	143.4
6	27.47	30.76	42.8	117

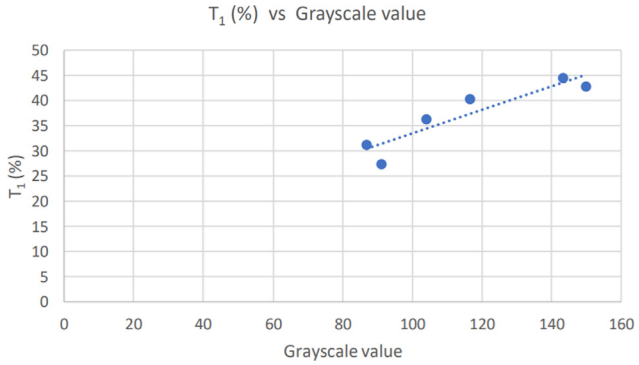

Fig. 2. T_1 (%) versus grayscale value.

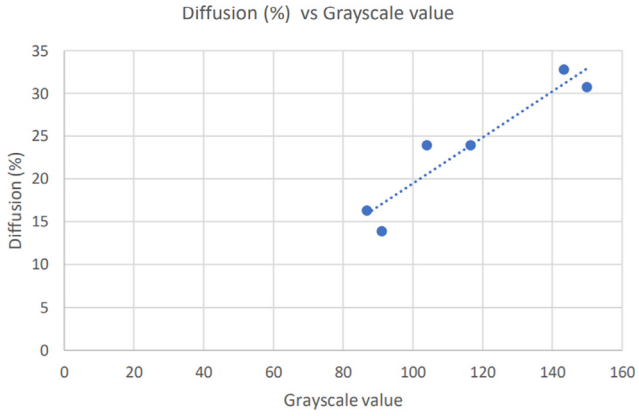

Fig. 3. Diffusion (%) versus grayscale value.

tent in NMR measurements and vice versa. This means that the accuracy reproducibility of MDs based on the three techniques T_1, T_2 and diffusion are reliable.

Fig. 12 demonstrate the effect of echo Time on The resolution of the ILP decay. Three scans with three different TE values were performed on the first sample in order to observe the best TE value that would resolve the water and fat peaks in the ILP spectrum. The ILP decay curve with TE = 700 μs was adopted for subsequent T_2 scans since it displayed no overlaps between the water and fat peaks (Fig. 12). As such, it is evident that the selected of echo time (TE) of 700 μs was long enough to show distinctive water and fat peaks for the breast samples under investigation. In contrast, Huang et al. (2018) could not discriminate between the water

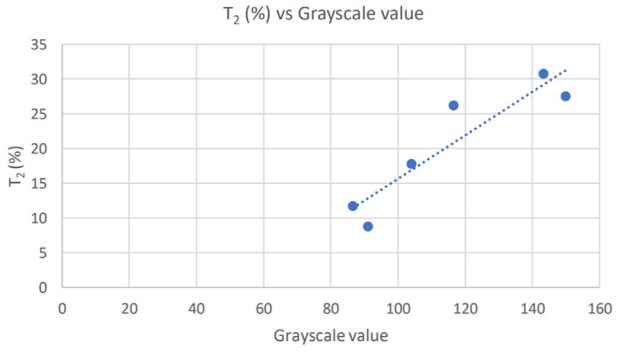

Fig. 4. T_2 (%) versus grayscale value.

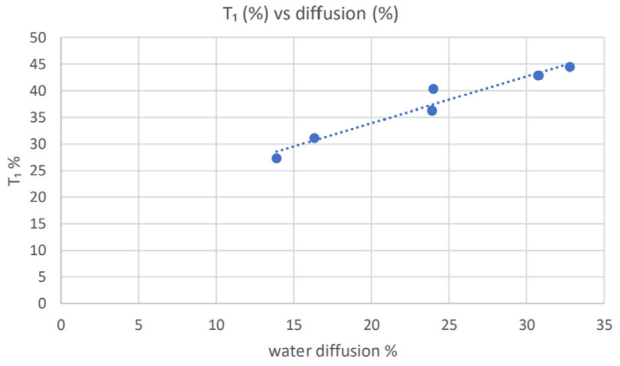

Fig. 5. Diffusion (%) versus T_1 (%).

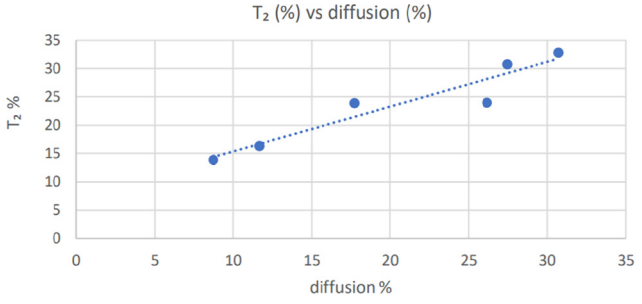

Fig. 6. T_2 (%) versus Diffusion (%).

and fat peaks due to the short CPMG echo time adopted (60 μs) leading to an overlap of water and fat peaks in the ILPs of T_2 spectra. This, indeed, reduces the accuracy of calculating the amplitude

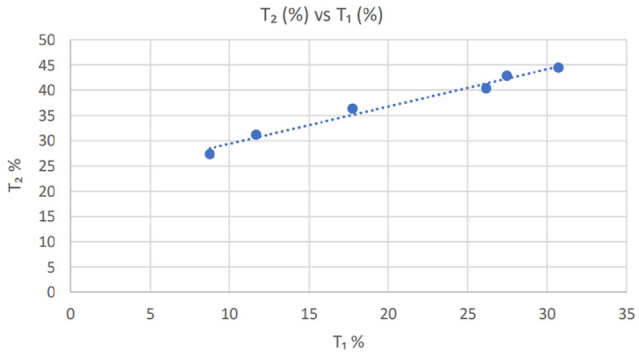

Fig. 7. T_2 (%) versus T_1 (%).

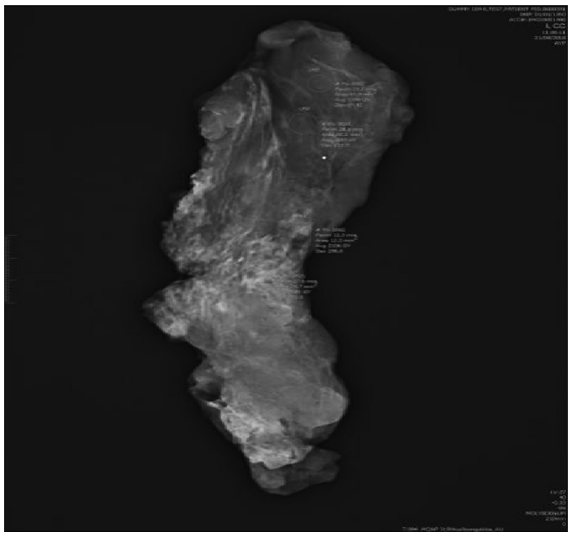

Fig. 8. Mammogram image of the first sample of breast tissue.

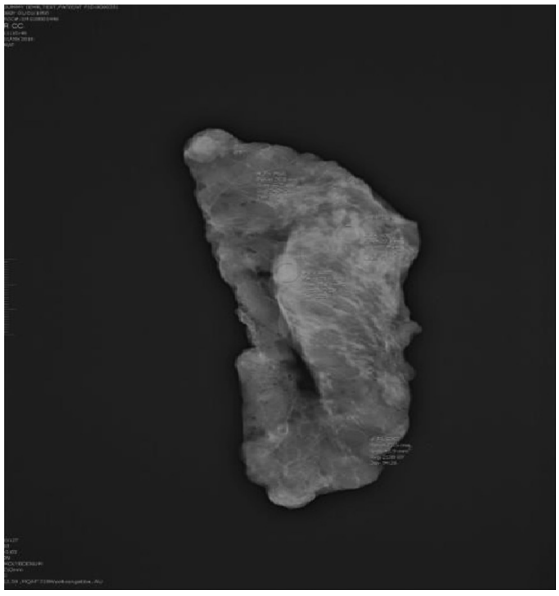

Fig. 9. Mammogram image of the second sample of breast tissue.

of water peaks in T_2 spectra. Consequently, the superiority of the present measurements is a direct result of the choice of the sequence parameters.

Evidently, all the experimental T_1 curves are bioexponental; they reveal the amount of water and fat in the breast tissue. In contrast, the study conducted by Tourell et al. (2018) did not reveal the amplitudes of the two components since the T_1 curves were mono-exponential. The measurements were based on the apparent T_1 of HMD and LMD regions. However, the current study has successfully determined the amplitudes of the two components. From the analysis, the water/fat ratio can be deduced from T_1 measurements, or the three techniques altogether.

In the water and fat peaks in T_2 spectra, it is possible to discriminate between the LMD, HMD, and intermediate MD regions of the excised samples. The HMD regions represent relatively larger amount of water molecules. This means that the transverse coherent magnetization components of protons in water molecules are highest in the HMD regions, followed by the intermediate MD, and then, the LMD regions. These differences are reflected in the water and fat peaks of the T_2 spectra. The analysis has also revealed that the water-to-fat ratio increases as the MD of excised breast samples increases. Overall, the experimental analysis has quantitatively shown that the pulse sequences can be used in the portable NMR instrument to provide quantitative measurements of MD on a continuous scale throughout the breast tissue sample. The measurements revealed more intricate details of breast tissue composition than the ones based on paired LMD/HMD classifications as reported by Tourell et al. (2018). Among the limitations of the current study is that it measured MD from the excised samples of participants undergoing prophylactic mastectomy, and hence, it is unclear whether the outcomes provide representative measurements for patients in both the upper and lower MD quartile of the BI-RADs scale. Further, the ILP might have introduce numerical errors while reconstructing the T_2 distributions, thereby reducing the accuracy of T_2 measurements. This problem was recently reported by Ali et al. (2019). Possibly, the L-bend was not always identifiable due to the effect of noise in the data. Most likely, the T_2 distributions were either under- or over-smoothened, especially where sub-optimal ILT values were observed. Such errors stem from the ILT framework employed, which should be investigated in future studies. Nevertheless, this research is novel in the sense that it represents the first time when T_1, T_2, and NMR diffusion are employed sequentially for each region of interest to quantitatively measure the distribution of MDs in breast tissue samples.

5. Conclusion

This research has demonstrated that the three techniques (T_2, T_1, and NMR-aided diffusion) are fairly in agreement with one other in quantifying HMD, intermediate MD, and LMD regions of breast tissue sample. Certainly, these regions, which represent changes in MD, are useful quantitative indicators of breast cancer progression stages. Furthermore, the outcomes lend support to the utilization of NMR probes to quantify MD affordably and conveniently. The method is also safe since it is free from ionizing radiation. The impressive correlation between the measurements indicate the fundamental essence of selecting the portable-NMR parameters for measuring MD. The results have important implications in clinical settings and more so, to breast cancer patients. For instance, they can be used in the early prediction of MD and subsequent risk analysis of breast cancer. The study could also be

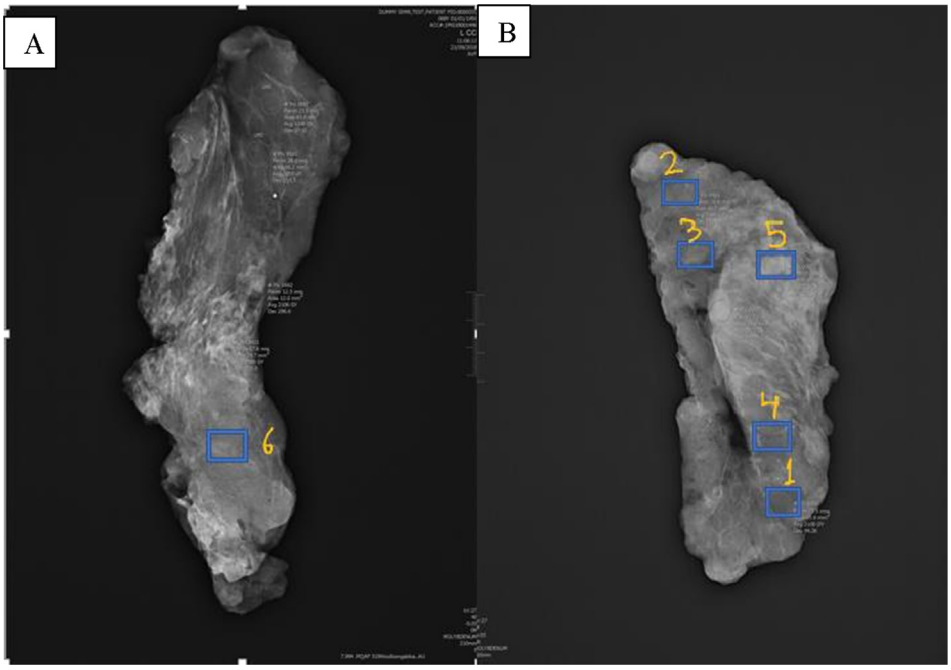

Fig. 10. Regions of interest of the (a) first and (b) second samples.

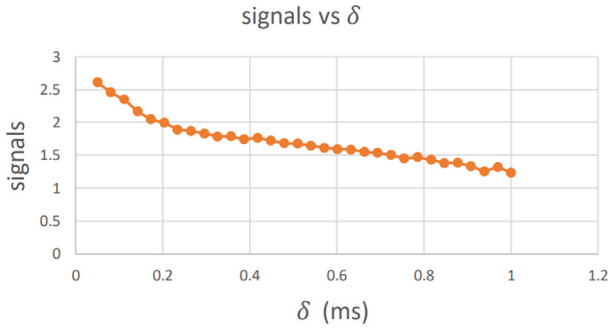

Fig. 11. Graphical representative measurement for the Diffusion (D) technique.

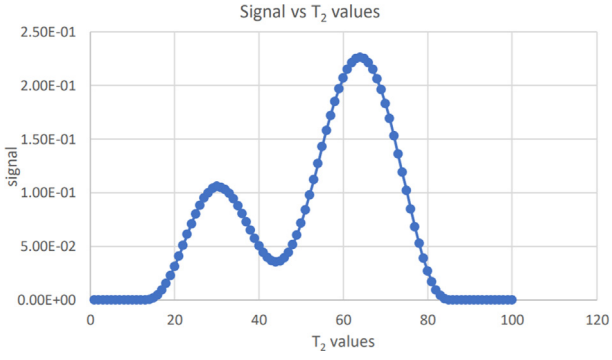

Fig. 12. ILP decay with TE = 700 μs (region 6).

extended to predicting the utility of hormonal therapy with the view of preventing breast cancer.

Declaration of Competing Interest

The authors declare that they have no known competing financial interests or personal relationships that could have appeared to influence the work reported in this paper.

Acknowledgement

The authors gratefully acknowledge The Deanship of Scientific Research (DSR) at King Abdulaziz University, Jeddah DSR for technical and financial support under grant no. RG-87-135-42.

References

Aiello, E., Buist, D., White, E., Porter, P., 2005. Association between mammographic breast density and breast cancer tumor characteristics. Cancer Epidemiol. Biomark. Prev. 14 (3), 662–668. https://doi.org/10.1158/1055-9965.epi-04-0327.

AIHW, 2017. Australian Cancer Incidence and Mortality (ACIM) Books: Breast Cancer. Australian Institute of Health and Welfare, Canberra, Australia.

Ali, T.S., Tourell, M.C., Hugo, H.J., Pyke, C., Yang, S., Lloyd, T., Momot, K.I., 2019. Transverse relaxation-based assessment of mammographic density and breast tissue composition by single-sided portable NMR. Magn. Reson. Med. https://doi.org/10.1002/mrm.27781.

Bell, R.J., 2020. Mammographic density and breast cancer screening. Climacteric. 23 (5), 460–465. https://doi.org/10.1080/13697137.2020.

Bluemich, B., Perlo, J., 2008. Mobile single-sided NMR. Prog. Nucl. Magn. Reson. Spectrosc. 52 (4), 197–269. https://doi.org/10.1016/j.pnmrs.2007.10.002.

Brentnall, A.R., Harkness, E.F., Astley, S.M., Donnelly, L.S., Stavrinos, P., Sampson, S., Evans, D.G., 2015. Mammographic density adds accuracy to both the Tyrer-Cuzick and Gail breast cancer risk models in a prospective UK screening cohort. Breast Cancer Res. 17 (1). https://doi.org/10.1186/s13058-015-0653-5.

Brinton, L.A., Gaudet, M.M., Gierach, G.L., 2018. (2018). Breast cancer. In: Thun, M., Linet, M.S., Cerhan, J.R., Haiman, C.A., Schottenfeld, D. (Eds.), Cancer Epidemiology and Prevention. Oxford University Press, pp. 861–888.

Britt, K.L., Cuzick, J., Phillips, K.A., 2020. Key steps for effective breast cancer prevention. Nat. Rev. Cancer. 20 (8), 417–436.

Butler, R.S., 2015. Invited commentary: The breast density dilemma–challenges, lessons, and future directions. Radiographics 35, 324–326.

Catherine, W., John, T., 2019. MRI in Practice. John Wiley & Sons Ltd., Oxford, UK.

Cil, T., Fishell, E., Hanna, W., Sun, P., 2010. Mammographic density and the risk of breast cancer recurrence after breast-conserving surgery. Breast Dis.: A Year Book Quart. 21 (3), 226–227. https://doi.org/10.1016/s1043-321x(10)79560-6.

Collaborative Group on Hormonal Factors in Breast Cancer, 2012. Menarche, menopause, and breast cancer risk: Individual participant meta-analysis, including 118 964 womenwith breast cancer from 117 epidemiological studies. Lancet Oncol. https://doi.org/10.1016/S1470-2045(12)70425-4.

Dale, B.M., Brown, M.A., Semelka, R.C., 2015. MRI: Basic Principles and Applications. John Wiley & Sons Ltd, NY.

Danieli, E., Blümich, B., 2013. Single-sided magnetic resonance profiling in biological and materials science. J. Magn. Reson. 229, 142–154. https://doi.org/10.1016/j.jmr.2012.11.023.

Eriksson, L., Czene, K., Rosenberg, L., Humphreys, K., Hall, P., 2013a. Possible influence of mammographic density on local and locoregional recurrence of breast cancer. Breast Cancer Res. 15 (4). https://doi.org/10.1186/bcr3450.

Eriksson, L., Czene, K., Rosenberg, L.U., Törnberg, S., Humphreys, K., Hall, P., 2013b. Mammographic density and survival in interval breast cancers. Breast Cancer Res. 15 (3). https://doi.org/10.1186/bcr3440.

Ghosh, K., Brandt, K.R., Reynolds, C., Scott, C.G., Pankratz, V.S., Riehle, D.L., Vachon, C. M., 2011. Tissue composition of mammographically dense and non- dense breast tissue. Breast Cancer Res. Treat. 131 (1), 267–275. https://doi.org/10.1007/s10549-011-1727-4.

Huang, X., 2018. Quantification of breast tissue density: correlation between single-sided portable NMR and micro-CT measurements. Radiology, 03–20.

Huo, C.W., Chew, G., Hill, P., Huang, D., Ingman, W., Hodson, L., Britt, K., 2015. High mammographic density is associated with an increase in stromal collagen and immune cells within the mammary epithelium. Breast Cancer Res. 17 (1). https://doi.org/10.1186/s13058-015-0592-1.

Liu, J., Liu, P.F., Li, J.N., Qing, C., Ji, Y., Hao, X.S., Zhang, X.N., 2014. Analysis of mammographic breast density in a group of screening chinese women and breast cancer patients. Asian Pac. J. Cancer Prev. 15 (15), 6411–6414.

Mccormack, V.A., 2006. Breast density and parenchymal patterns as markers of breast cancer risk: a meta-analysis. Cancer Epidemiol. Biomark. Prev. 15 (6), 1159–1169. https://doi.org/10.1158/1055-9965.epi-06-0034.

National Cancer Institute, 2017. In: Howlader et al., (Eds), SEER Cancer Statistics Review, 1975–2014. NCI, Bethesda, MD.

National Health and Medical Research Council, 2018. Australian Code for the Responsible Conduct of Research. Retrieved May 06, 2019, from https://nhmrc.gov.au/about- us/publications/australian-code-responsible-conduct-research-2007.

Momot, K., 2019. Wolfram Mathematica program. Wolfram Research, Inc. (www.wolfram.com), Mathematica Online, Champaign, IL, USA.

Niell, B.L., Freer, P.E., Weinfurtner, R.J., Arleo, E.K., Drukteinis, J.S., 2017. Screening for breast cancer. Radiol. Clin. North Am. 55 (6), 1145–1162. https://doi.org/10.1016/j.rcl.2017.06.004.

Iranmakani, S., Mortezazadeh, T., Sajadian, F., et al., 2020. A review of various modalities in breast imaging: technical aspects and clinical outcomes. Egypt. J. Radiol. Nucl. Med. 51, 57. https://doi.org/10.1186/s43055-020-00175-5.

Kopans, D., 2009. High mammographic breast density is independent predictor of local but not distant recurrence after lumpectomy and radiotherapy for invasive breast cancer. Breast Dis.: A Year Book Quart. 20 (3), 280–281. https://doi.org/10.1016/s1043- 321x(09)79340-3.

Karim, S., Malik, I.R., Nazeer, Q., et al., 2019. Molecular analysis of V617F mutation in Janus kinase 2 gene of breast cancer patients. Saudi J. Biol. Sci. 26 (6), 1123–1128.

Salem, C., Atallah, D., Safi, J., Chahine, G., Haddad, A., El Kassis, N., Maalouly, L.M., Moubarak, M., Dib, M., Ghossain, M., 2017. Breast density and breast cancer incidence in the lebanese population: results from a retrospective multicenter study. Biomed Res. Int. 2017, 7594953. https://doi.org/10.1155/2017/7594953.

Sickles, E., 2013. Mammography. In: ACR BI-RADS® Atlas, Breast Imaging Reporting and Data System. American College of Radiology, Reston, VA. Retrieved 5 1, 2019, from https://www.acr.org/-/media/ACR/Files/RADS/BI-RADS/BIRADS-Reference- Card.pdf.

Shang, M.Y., Guo, S., Cui, M.K., Zheng, Y.F., Liao, Z.X., Zhang, Q., Piao, H.Z., 2021. Influential factors and prediction model of mammographic density among Chinese women. Medicine 100, (28), e26586. https://doi.org/10.1097/MD.0000000000026586.

Stone, J., Dite, G., Gunasekara, A., Englishetal, D., 2006. The heritability of mammographically dense and nondense breast tissue. Cancer Epidemiol. Biomark. Prev. 15 (4), 612–617. https://doi.org/10.1158/1055-9965.epi-05-0127.

Sulieman, A., Serhan, O., Al-Mohammed, H.I., Mahmoud, M.Z., Alkhorayef, M., Alonazi, B., Manssor, E., Yousef, A., 2019. 2019.Estimation of cancer risks during mammography procedure in Saudi Arabia. Saudi J. Biol. Sci. 26 (6), 1107–1111.

Sung, H., Ferlay, J., Siegel, R.L., Laversanne, M., Soerjomataram, I., Jemal, A., Bray, F., 2021. Global cancer statistics 2020: GLOBOCAN estimates of incidence and mortality worldwide for 36 cancers in 185 countries. CA Cancer J. Clin. 71 (3), 209–249. https://doi.org/10.3322/caac.21660.

Tamam, N., Salah, H., Rabbaa, M., Abuljoud, M., Sulieman, A., Alkhorayef, M., Bradley, D.A., 2021. Evaluation of patients radiation dose during mammography imaging procedure. Radiat. Phys. Chem. 188. 109680, 1–5.

Tourell, M.C., Ali, T.S., Hugo, H.J., Pyke, C., Yang, S., Lloyd, T., Momot, K.I., 2018. T1-based sensing of mammographic density using single-sided portable NMR. Magn. Reson. Med. 80 (3), 1243–1251. https://doi.org/10.1002/mrm.27098.

Tyrer, J., Duffy, S.W., Cuzick, J., 2004. A breast cancer prediction model incorporating familial and personal risk factors. Stat. Med. 23 (7), 1111–1130. https://doi.org/10.1002/sim.1668.

Venkataramanan, L., Song, Y., Hurlimann, M., 2002. Solving Fredholm integrals of the first kind with tensor product structure in 2 and 2.5 dimensions. IEEE Trans. Signal Process. 50 (5), 1017–1026. https://doi.org/10.1109/78.995059.

White, E., Velentgas, P., Mandelson, M., Lehman, C., 1998. Variation in mammographic breast density by time in menstrual cycle among women aged 40–49 years. JNCI J. Natl. Cancer Inst. 91 (1), 90. https://doi.org/10.1093/jnci/90.12.906.

Woolcott, C.G., Koga, K., Conroy, S.M., Byrne, C., Nagata, C., Ursin, G., Maskarinec, G., 2012. Mammographic density, parity and age at first birth, and risk of breast cancer: an analysis of four case–control studies. Breast Cancer Res. Treat. 132 (3), 1163–1171. https://doi.org/10.1007/s10549-011-1929-.